Analysis of near field sound radiation from a resonant unbaffled plate using simplified analytical models

Murat Inalpolat[a], Mehmet Caliskan[b] and Rajendra Singh[c]

(Received: 22 April 2009; Revised: 4 December 2009; Accepted: 31 December 2009)

Near field radiation behavior of an unbaffled square plate with free edges, which is excited by a harmonic force at its midpoint, is analytically, computationally and experimentally studied. Emphasis is on the applicability of simplified analytical models to predict the near field sound pressures and spatially-averaged surface and acoustic intensities. First, the plate is computationally discretized into equal segments that are replaced by simple, phase-correlated discrete acoustic sources. Piston radiator models (with and without mutual radiation impedance terms) as well as pulsating sphere models are employed to exhibit the contribution of mutual impedance terms. The near field pressure and spatially-averaged intensity radiated from phase-correlated discrete sources are calculated based on the premise that their individual phases are obtained from the plate (surface) vibration measurements. The importance of mutual impedance terms on the near field radiation is highlighted. Second, the two-microphone acoustic intensity and the surface intensity techniques are employed to determine the spatially-averaged intensity spectra, like analytical models. Results are examined on both narrow and 1/3 octave band bases up to 1600 Hz covering radiation from several plate vibration modes. Finally, an indirect boundary element model is used to predict spatially-averaged intensity spectra, as well as to simulate the two-microphone method given surface vibration data. All predictions are compared with analogous measurements. Discrepancies between theory and experiments (and even between two intensity measurements) are discussed along with possible sources of error.

Primary subject classification: 23.1; Secondary subject classification: 42

1 INTRODUCTION

Near field radiation information is often needed to quantify relatively noisy source regions, radiation paths, and acoustic "short-circuiting"[1]. In particular, this could be helpful in understanding the sound radiation from thin, resonant plates, which have relatively light structural damping and typically found in machinery casings[2,3]. However, the near fields of resonant plates with classical boundaries (such as free edges) have been studied by only a few researchers[4–7]. Accordingly, a thin, steel square plate (with free boundaries) with inherently light structural damping is chosen as the example in our study. Such structures are routinely examined in industry; examples include modal testing as well as sound pressure to force (or acceleration) type frequency response function measurements that are routinely conducted under freely suspended conditions[8–10]. Since a closed form solution for sound radiation for this structure with free boundaries is not available, we will apply simplified analytical, computational and experimental methods with focus on the near field acoustics. In particular, analytical models with phase correlated discretized sources are developed to examine the role and the relative contribution of both self and mutual radiation impedance terms. Further, an indirect boundary element formulation (BEM) is used to predict spatially-averaged sound intensity as well to assess possible errors in the analytical or the experimental methods employed. The spatially-averaged intensity is measured at discrete points over the top

[a] Gear and Power Transmission Research Laboratory, The Ohio State University, Columbus, OH 43210, USA; email: inalpolat.1@osu.edu.
[b] Department of Mechanical Engineering, Middle East Technical University, 06531 Ankara, TURKEY; email: caliskan@metu.edu.tr.
[c] Acoustics and Dynamics Laboratory, The Ohio State University, Columbus, OH 43210, USA; email: singh.3@osu.edu.

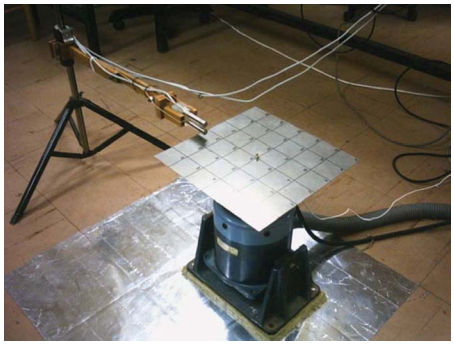

Fig. 1—Example case (free-free steel plate) and near-field acoustic intensity (I_m) measurements.

surface of the plate examined in the experimental aspects of the study. This scalar quantity permits us to easily compare measurements with analytical predictions. Further, the spatially-averaged intensity over a limited control surface can be used to examine modal vibro-acoustic behavior of plate structures, evaluate structural-acoustics type transfer function measurements at limited field locations, and conduct structural design and noise control studies over lower and mid frequency regimes (such as the role of constrained or free layer damping treatments in reducing radiation). Nevertheless, the proposed simplified analytical models can be utilized to predict near and far field pressure and sound power spectra given phase correlated surface velocities. Overall, the main goal of this article is to comparatively evaluate the methods and to demonstrate their applicability to a problem of significant interest from the machinery noise reduction perspective. On a more fundamental basis, we also pose an interesting (and perhaps even a benchmark) problem for researchers and practitioners.

2 PROBLEM FORMULATION

The scope of the investigation is limited by the following: 1. A thin square plate (300 mm $\times$ 300 mm $\times$ 1 mm) is chosen as the example since elastic plates are found in many engineering applications. The example case is shown in Fig. 1; the free-free steel plate is excited by a point force at its midpoint ($x=0, z=0$). 2. No baffle is intentionally considered in our study to simulate industrial test conditions and corresponding possible errors in measurements or modeling. 3. Both narrow band (particularly at resonance frequencies) and 1/3 octave-band spectra of spatially-averaged sound intensity up to 1600 Hz are considered. 4. Measurements and simulations were carried out in both geometric and acoustic near fields at all resonance frequencies within the analysis range[11]. Main objectives of this study are thus to: (a) explore the applicability of discrete sound source models as well as conventional intensity measurement methods to assess the near field radiation by a resonant plate and examine the role of mutual impedance terms; and (b) Comparatively evaluate analytical, computational and experimental methods in terms of sound radiated by resonance modes.

Table 1 lists five analytical and computational models that are employed to predict spatially-averaged sound intensity ($\bar{I}$); note that the usage of a scalar quantity (such as $\bar{I}$) permits us to easily compare methods though these methods can be employed to examine other radiation properties as well. First, three analytical discrete source models are employed to predict the near field radiation[12–16]. In particular, two

Table 1—Overview of the analytical and computational methods employed to predict or measure spatially-averaged sound intensity ($\bar{I}$).

Model	Model Type	Mutual Interactions Between Sources	Brief Description
Model A1	Baffled-piston radiator	Excluded	Intended for far field estimations
Model A2	Baffled-piston radiator	Included	Intended for near field estimations
Model B	Pulsating sphere	Excluded	Expected to give a rough estimation
Model C1	Indirect BEM	Included	Generates results comparable to the discrete models
Model C2	I_m simulation by BEM	Included	To examine the near field radiation and errors in modeling

models (*A1 and B*) do not incorporate any interactions between discrete sources on the plate surface, but *Model A2* does and it is utilized to examine the influence of mutual interactions on the near field radiation. Further explanation of these models will be given in Sec. 3. Laboratory experiments are carried out to assist and assess the discrete radiation models. Both two-microphone acoustic intensity (I_m) and surface intensity (I_s) measurement techniques are applied to determine the spatially-averaged intensity $\bar{I}$ from the top surface of the plate, as shown in Fig. 1. However, the measured narrow band spectra from these two techniques are not very close. To examine the underlying reasons that cause such differences, discrete radiation models are re-examined along with two computational models (*C1 and C2*) based on the indirect boundary element method (BEM). The BEM models are also used to investigate the near field effects.

3 NEAR FIELD PREDICTIONS BY ANALYTICAL (DISCRETE RADIATOR) MODELS

Discrete sound source models are widely used to predict radiation from relatively simple structures; for example, refer to the book[16] by Koopmann and Fahnline that includes many examples. However, the authors calculate radiation from either idealized or "controlled" sources. Nevertheless, such simplified source calculations can even be extended to more advanced sound power estimation techniques. For instance, Hill et al. employ acoustic multi-poles to decompose an independent set of radiating functions for estimating sound power of three-dimensional complex acoustic sources[17].

Consider Fig. 2, where the concept of self and mutual radiation is illustrated in terms of two discrete radiators (i and j). In particular, surface velocity U_i of the i^{th} piston as described in Fig. 2(b) affects pressure P_j and thus power W_j of the j^{th} piston; this indicates mutual interactions between two radiators. Both discrete sources also radiate independently directly into their half-space as shown in Fig. 2(a). The complex-valued radiation impedance Z_{ij} (in force to velocity units) at frequency f (Hz) is given as $Z_{ij}(f)=F_i(f)/U_j(f)=R_{ij}(f)+jX_{ij}(f)$, where F_i is the radiation force generated on the i^{th} discrete structure (or region) by the surface velocity U_j of the j^{th} discrete region[18–25]. Here, R_{ij} is the radiation resistance and X_{ij} is the radiation reactance, where self and mutual impedance terms are given by Z_{ii} and Z_{ij}[14,18–20,22,26].

In our study, three different analytical models are used with phase-correlated and interacting sources on the plate. Firstly, two vibrating piston source models (*A1* and *A2*) are used to understand the influence of Z_{ij} terms. Second, a pulsating sphere formulation (B) (with Z_{ii} terms only) is used. Predictions with Model A1 and Model B allow us to determine the difference between these two models. Further, Model A2 permits us to compare the predictions with and without mutual impedance terms, thus exhibiting the relative contribution of mutual impedance terms.

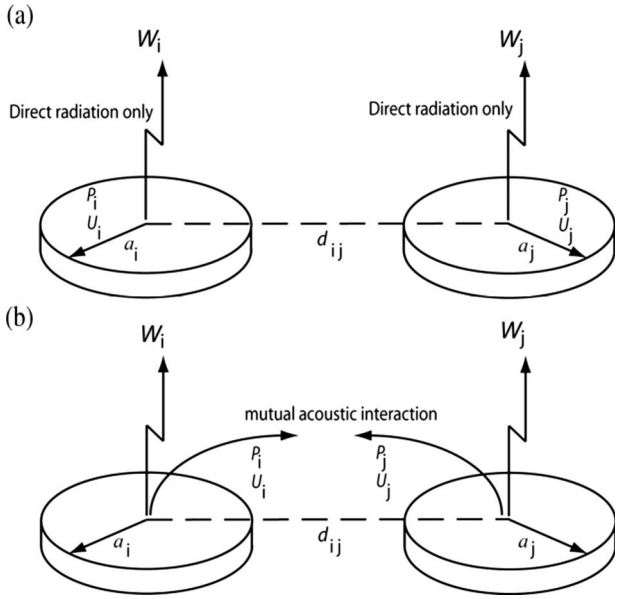

Fig. 2—Illustration of the discrete acoustic models. (a) Without mutual interactions and (b) with mutual interaction between sources (given by i and j).

3.1 Discrete Piston Radiator Sources and the Effect of Mutual Interactions

The plate is discretized into $N=36$ segments ($\Delta x_s = \Delta z_s = 0.05$ m) as shown in Fig. 3. Then a vibrating circular piston (assumed to be in an infinite baffle) is placed at the center of each segment. *Model A1* includes phase relations among the vibrating segments; their relative phase spectra are obtained via vibration measurements at $N=36$ discrete points; this model excludes the mutual radiation impedance effects[19,20]. In *Model A1*, each segment of area S_i is replaced by a circular vibrating piston (of radius a_i and $S_i=\pi a_i^2$) radiating with its own phase. Here, the subscript i refers to the i^{th} discrete element (segment) on the plate. The reason for using 36 partitions is that the two-microphone intensity (I_m) measurements showed that an increase in the number of segments (N) beyond 36 provided marginal improvement to the $\bar{I}$ spectrum (as discussed later in Sec. 4). In this study, spatially-averaged intensity ($\bar{I}$) is defined as:

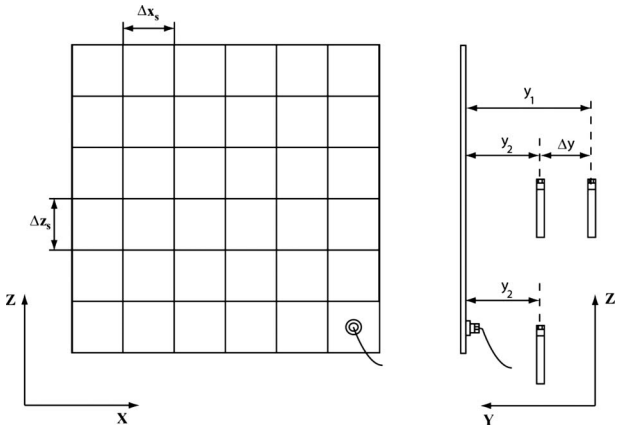

Fig. 3—Schematic of the plate (including discretized elements on the surface) and intensity measurements (using both surface and 2-microphone method). Microphones in the near field along with an accelerometer on the surface are shown in the Cartesian coordinate system.

$$\bar{I}(\omega) = \frac{\sum_{i=1}^{N} I_i(\omega) S_i}{\sum_{i=1}^{N} S_i}, \qquad (1)$$

Here, I_i is the intensity measured or predicted at the mid point of a partition (or piston) i located at the top side of the plate and S_i is the corresponding partition (piston) area. Further, N is the total number of segments used to model the radiation from the top surface of the plate; we have selected N=36. The aim here is to study the near field radiation over a selected field segment (from the top surface of the plate) and not to calculate the power radiated from the plate including its edges. The expression for far field intensity (I) for the i^{th} piston at frequency f is given by:

$$I_i(\omega) = 0.5 U_i(\omega)^2 \rho_o c_o (1 - 2J_1(\Gamma)/\Gamma), \qquad (2)$$

where $\Gamma = 2ka_i$, U_i is surface velocity (measured on segment i), ρ_o is the density (air), c_o is the speed of sound, k is the wave number and J_1 is the Bessel function (first order)[19,21,26]. The pressure amplitude distribution on the face of a baffled piston ($P(\kappa)$), where j is the imaginary unit and κ is an arbitrary point on the radiating piston, is given as follows[20,21].

$$P(\kappa) = ((jk\bar{P})/2\pi) \int_{-\pi/2}^{\pi/2} d\theta \int_{0}^{2r_1 \cos(\theta)} (e^{-jk\ell}/\ell)\, \ell\, d\ell. \qquad (3)$$

Two infinitesimal elements are arbitrarily chosen on the surface of the piston radiator. One of these infinitesimal areas (dS_1) is exactly at point κ and the other one ($dS_2 = \ell\, d\ell\, d\theta$) is at point δ, which is at distance ℓ and angle θ with respect to point κ; note that θ is the angle between the line connecting point κ and piston center and the line connecting point κ to point δ. Here, $dS_1 = r_1 dr_1 d\tau$ where r_1 is the distance (radius) from point κ to the piston center, and τ is the polar angle of point κ with respect to the piston center. The limits of the second integral are the ends of the vector connecting the points (κ and δ). Note also that dS_2 is already explicitly included in the free field Green's function ($e^{-jk\ell}/\ell$). Finally, $\bar{P}$ is the pressure amplitude on the piston surface in the above integration. The total acoustic force exerted on the piston is given by[19,20] $F_i = \int P(\kappa) dS_1$. The self-radiation impedance, $Z_{ii} = F_i / U_i$, is thus found as follows, where H_1 is the Struve function (first order):

$$Z_{ii}(\omega) = \rho_o c_o S_i \left[1 - \left(\frac{2J_1(\Gamma)}{\Gamma} \right) + j \left(\frac{2H_1(\Gamma)}{\Gamma} \right) \right]. \qquad (4)$$

The total spatially-averaged intensity is finally found by a superposition of the results from 36 sources. Next, *Model A2* is formulated with mutual radiation terms. The mutual impedance (Z_{ij}) terms[20,22,23] are defined as follows where d_{ij} is the distance between the i^{th} and the j^{th} pistons and k is the wave number:

$$Z_{ij}(\omega) = ((\rho_o c_o k^2 S_i S_j)/2\pi) \cdot [(4J_1(\Gamma/2))/\Gamma]^2 ((\sin(kd_{ij})/kd_{ij}) + j(\cos(kd_{ij})/kd_{ij})). \qquad (5)$$

The spatially-averaged intensity at any frequency ω by the i^{th} piston radiator (with combined self and mutual impedances) is calculated as follows, where Re is the real part of a complex-valued expression and $*$ indicates complex-conjugate of a complex variable:

$$I_i(\omega) = \mathrm{Re}(Z_{ii}(\omega)/S_i) |U_i(\omega)|^2 + \sum_j \mathrm{Re}(Z_{ij}(\omega) U_i(\omega) U_j^*(\omega)/S_i S_j). \qquad (6)$$

Then $\bar{I}$ is found by a superposition of individual I_i terms as given in Eqn. (1). In our study, Struve Function is approximated by the following simplified expression[24], where $\beta = 1/\pi$ and J_0 is the Bessel function (zeroth order). This particular expression reduces the computational time and programming effort.

$$H_1(\Gamma) = (2\beta) - J_0(\Gamma) + ((16\beta) - 5)(\sin(\Gamma)/\Gamma) + (12 - (36\beta))(1 - \cos(\Gamma)/(\Gamma)^2). \qquad (7)$$

3.2 Discrete Pulsating Sphere Sources (Without Mutual Interactions)

The pulsating sphere formulation (*Model B*) is employed next. Like *Model A1, Model B* is also expected to give a rough estimate since it excludes the mutual radiation effects. Each pulsating sphere (of radius a_i, restricted to half-space) formulation is given by the following[26], where ω is the angular frequency in rad/s:

$$I_i(\omega) = (\rho_o U_i(\omega)^2 a_i^2 \omega^2)/(4c_o(1 + (\Gamma/2)^2)) \qquad (8)$$

The spatially-averaged intensity over the plate from the plate is then found by summing up the individual intensities as given by Eqn. (8) from 36 phase-correlated segments.

3.3 Influence of the Mutual Impedance on Near-Field Radiation

The extent of geometric near field from the plate surface is theoretically given by the Rayleigh distance (D_R). It is defined as $D_R = ka^2/2$, where k is the wave number and a is half of the longest source dimension (say radius of a circular piston). The geometric near field distances for the plate under investigation are determined via D_R calculations corresponding to the plate dimensions as well as dimension of a single source segment over the applicable frequency range. The Rayleigh distance is found to be 0.012 m and 0.33 m at 1600 Hz for an individual piston source and the whole plate, respectively. Since both D_R values are less than 1, discrete analytical model calculations as well as the experiments were carried out in the geometric near field. Besides, acoustic near fields of simple sources can be theoretically determined by $kr < 1$ and in our case $kr \approx 0.5$ at the highest analysis frequency (1600 Hz). This ensures all the measurements and simulations were carried out in the acoustic near field. Also, note that the wavelength of the bending waves on the plate (critical frequency of the plate is $f_c \approx 13$ kHz) is calculated to be $0.076 \leqslant \lambda_b \leqslant 0.42$ m within the analysis frequency range,. It is larger than the characteristic dimensions of a single segment (0.05 m or $a_i = 0.028$ m) though it is comparable to the overall plate dimensions (0.3 m $\times$ 0.3 m).

The relative importance of self (Z_{ii}) and mutual (Z_{ij}) impedance terms on the radiation behavior is evaluated next. Radiation resistances (R_{ij}) and reactances (X_{ij}) are compared for the baffled circular piston models (36 sources on the plate surface). Predictions of *Model A2* are compared in Fig. 4(a) for R_{11} and R_{1j}, and in Fig. 4(b) for X_{11} and X_{1j} (where $j = 2 \ldots 6$). Observe the relative effects of self and mutual radiation resistances in Fig. 4(a), where ka_i is constrained between 0 and 1 (corresponding

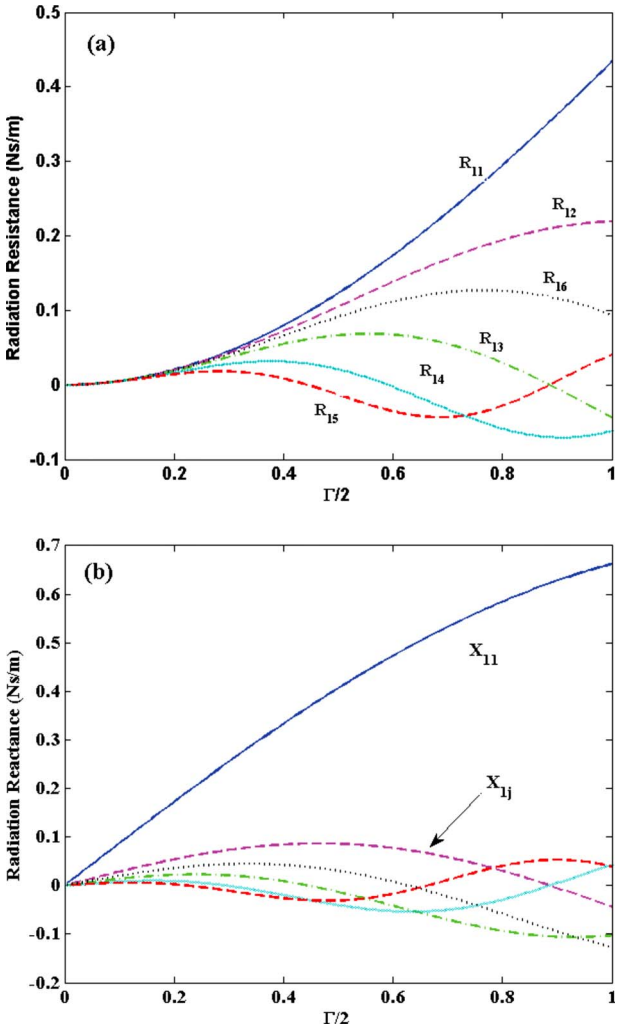

Fig. 4—Effect of self and mutual radiation impedance terms on the near field radiation behavior of the plate, where $\Gamma = 2ka_i$ and $j = 2 \ldots 6$. (a) Self (R_{11}) and mutual radiation resistance (R_{1j}); (b) Self (X_{11}) and mutual radiation reactance (X_{1j}).

to 0 and 1932 Hz respectively) and $ka_i = \Gamma/2$. Magnitude of the mutual resistance (R_{12}) between segments 1 and 2 is found to be almost equal to the self-resistance (R_{11}) in the range of $0 < \Gamma/2 < 0.4$ (corresponds to the upper frequency limit of 750 Hz). The other partitions exhibit the same effect as R_{11} of segment 1 up to $\Gamma/2 = 0.2$ (below 375 Hz). Though the resistances and reactances in our study are not normalized with respect to their surface area S_i, or separation distance d_{ij}, results illustrate the overall effects. The same procedure is repeated for the evaluation of the relative roles of self and mutual reactances on the radiation from segment-1. Resultant spectra for the near field range are given in Fig. 4(b). The role of mutual reactances on the overall radiation is found to be relatively less important even in the near field region.

In our study, 36 discrete sources are employed to simulate the sound field. Yet, the same plate is further

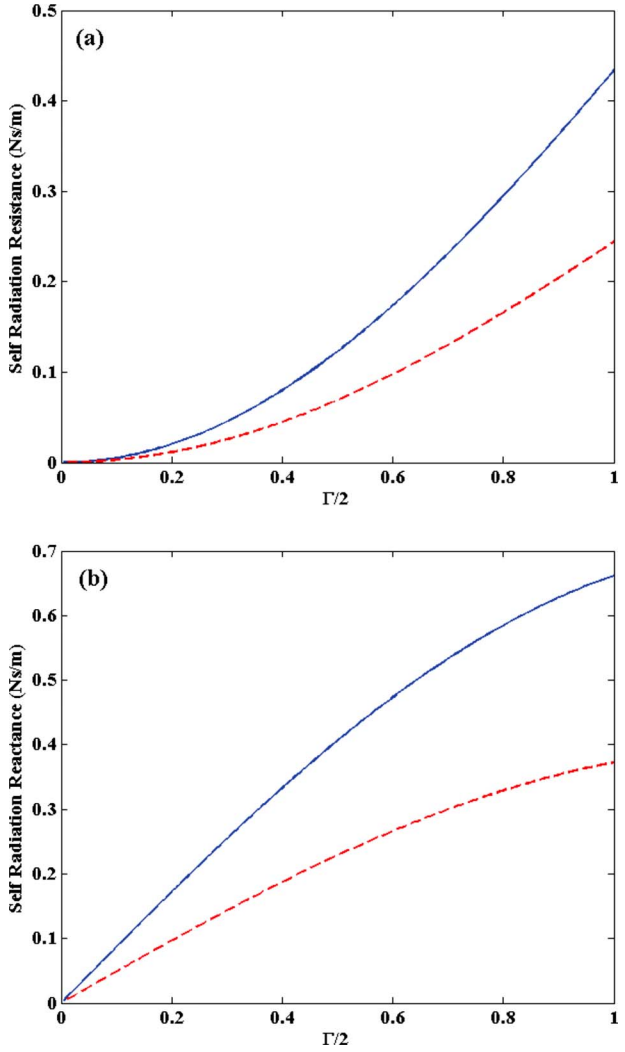

Fig. 5—Effect of number of plate segments (partitions) used on the near field radiation behavior, where $\Gamma = 2ka_i$. (a) Self-radiation resistance (R_{11}), and (b) self-radiation reactance (X_{11}). Key: (blue line) analysis for $N = 36$ segments, (red dashed line) analysis for $N = 64$ segments.

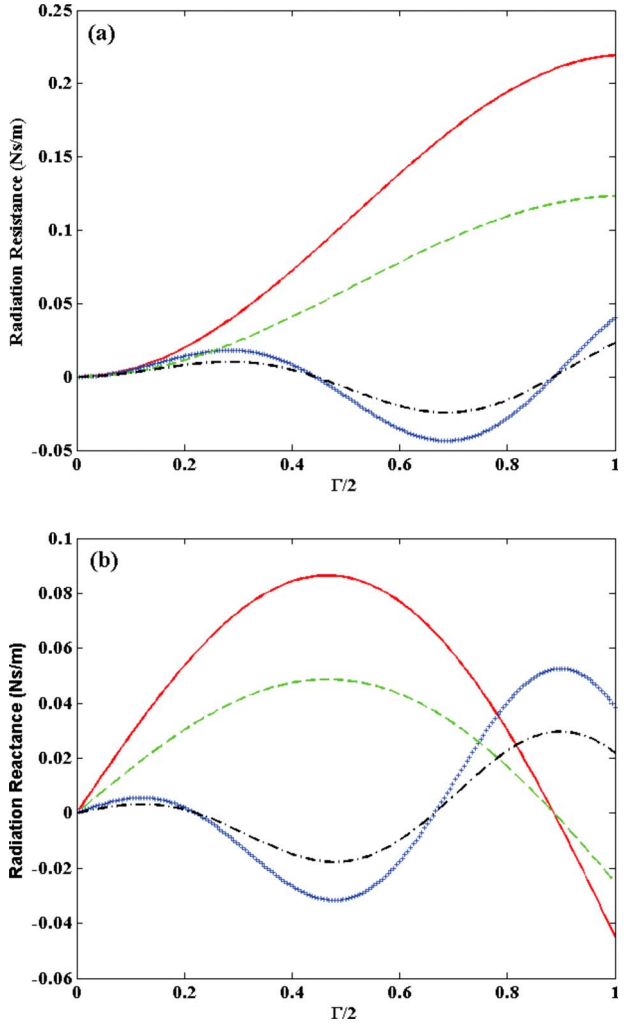

Fig. 6—Effect of number of plate segments (N) used on the impedance terms for $\Gamma = 2ka_i$ ($d_{12} \neq d_{15}$ and S_i differs). (a) Mutual radiation resistance [Key: (red line) R_{12} for 36 segments, (green dashed line) R_{12} for 64 segments, (blue crosses) R_{15} for 36 segments, (black dashed/dotted) R_{15} for 64 segments], and (b) mutual-radiation reactance [Key: (red) X_{12} for 36 segments, (green dashed line) X_{12} for 64 segments, (blue crosses) X_{15} for 36 segments, (black dashed/dotted) X_{15} for 64 segments].

divided into 64 geometrically identical baffled pistons. A near field based comparison of the self-resistance and the self-reactance terms of segment 1 of this plate with 36 and 64 segments are given in Figs. 5(a) and 5(b), respectively. As the number of discrete elements is increased, the effect of self-resistance is decreased by almost the same ratio (1.78 = 64/36). Consequently, the analytical model with 64 (or more) segments should be better as more elements contribute with a reduced weighting. However, the vibration velocity distribution (and their phases) now must be measured at 64 discrete points to have the benefit of a higher dimensional model.

Effect of mutual resistance and reactance terms are further explored for two different configurations. First, R_{12} (between segments 1 and 2) and then R_{15} (between segments 1 and partition 5) are compared in Fig. 6(a). Mutual resistances decrease as the separation distance (d_{ij}) increases, as expected. However, the frequency of resistance oscillations increases as the mutual effect of a piston further away is considered as reported by Stepanishen[27]. Such further neighbors of partition 1 can sometimes reduce the total fluid resistance on partition 1 because of higher frequency oscillations. Figure 6(a)

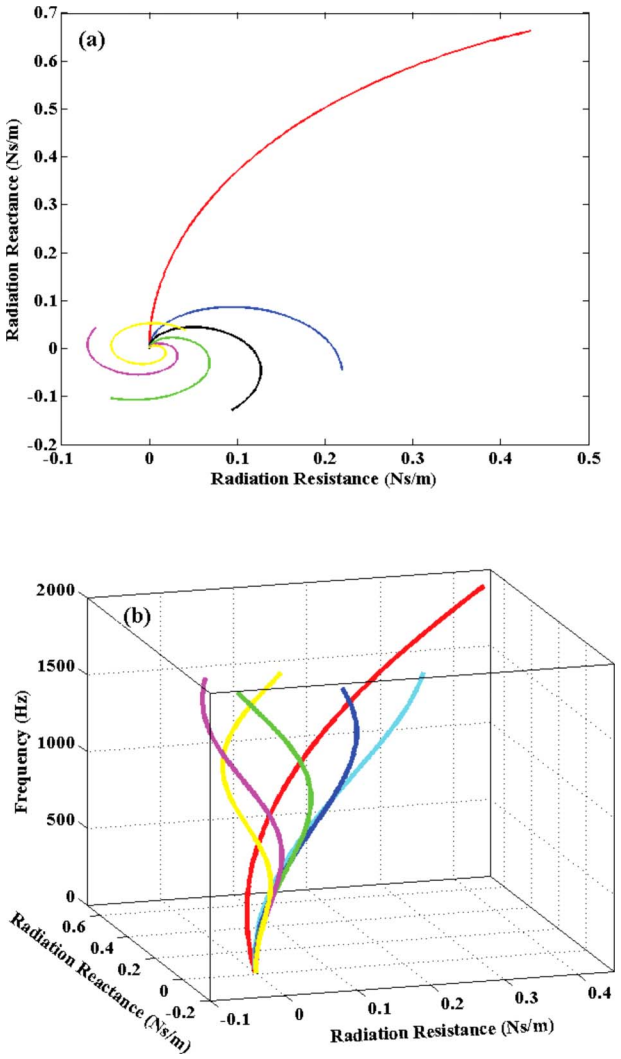

Fig. 7—Comparison of self and mutual radiation impedance terms using the Nyquist diagram. (a) Two dimensional plot, and (b) three dimensional plot. [Key: (red) Z_{11}, (blue) Z_{12}, (green) Z_{13}, (magenda) Z_{14}, (yellow) Z_{15}, (black) Z_{16} calculated for 36 segments and valid for part (a) and (b)].

shows that the $\mathrm{Re}(Z_{15})$ terms assume negative values in some regions in the near fields as they oscillate.

Similar observations can be made from Fig. 6(b) where oscillations may enhance or reduce the mass loading effect. For instance, the surface velocity of segment 2 tends to increase the mass loading on the surface of segment 1. But the surface velocity of segment 5 causes a reduction in the mass loading on segment 1 for both models. Obviously, these effects might change the effective natural frequencies of the "fluid loaded" plate, which is important when the near field radiation behavior changes. To aid the readers, two and three dimensional Nyquist plots are presented in Fig. 7. Self-radiation impedance (Z_{11}) is the dominant contributor to the acoustic response as depicted in Fig. 7(a). Further, Nyquist plots of Fig. 7(b) allow a better visualization of radiation resistances and reactances with an increase in frequency.

4 NEAR FIELD ACOUSTIC AND SURFACE INTENSITY MEASUREMENTS

The experimental set-up (Fig. 1) consists of sound intensity and surface intensity probes, two accelerometers with signal conditioners and two dynamic signal analyzers. An electro-dynamic shaker excites the plate through band-limited random or swept sine signals that are fed to the shaker by means of a power amplifier and a two-channel dynamic signal analyzer. The sound intensity probe is designed to hold two transducers (such as 12.5 mm phase-matched B&K 4165 condenser microphones) at an arbitrary angle for laboratory measurements; an effort was made to minimize the coefficient of reflection. The sound intensity I_m spectrum, at frequency ω (rad/s), is determined by using the well-known two-microphone expression[28]:

$$I_m(\omega) = (1/\omega\rho_o\Delta y)\mathrm{Im}(G_{P_2P_1}(\omega)). \qquad (9)$$

Here, G is the cross power spectrum between the two channels, P_2 and P_1 are the complex-valued pressure amplitudes at y_2 (closer to the measurement surface) and y_1 (at Δy from y_2) respectively, and ρ_o is the air density (1.205 $\mathrm{kg/m^3}$ at the room conditions). The side-by-side probe configuration (as shown in Figs. 1 and 3) is utilized for sound intensity measurements in the y direction (normal to the plate) with a separation of $\Delta y = 18$ mm in a plexiglass holder with a special arrangement that maintains Δy between the microphones. Acoustical center of the microphone (P_2) closer to the plate is at $y = 8$ mm from the surface of the plate; 64 ensemble averages are taken at each measurement point. Sound pressure and sound intensity calibrators are employed for the calibration of measurement microphones. Finally, the spatially-averaged intensity spectrum is calculated and expressed in dB re 1 $\mathrm{pW/m^2}$, both on narrow and 1/3 octave band basis.

The microphone at y_2 is used together with an accelerometer placed onto the plate to measure the surface intensity I_s, as schematically shown in Fig. 3. The microphone at y_2 is used together with an accelerometer located on the plate to measure the surface intensity I_s, as schematically shown in Fig. 3. Note that the accelerometer is placed at the center of each particular measurement point while the microphone was kept in close proximity to the surface above a measurement point. This procedure is repeated for $N = 36$ segments of the plate. The surface intensity is expressed by[29,30]

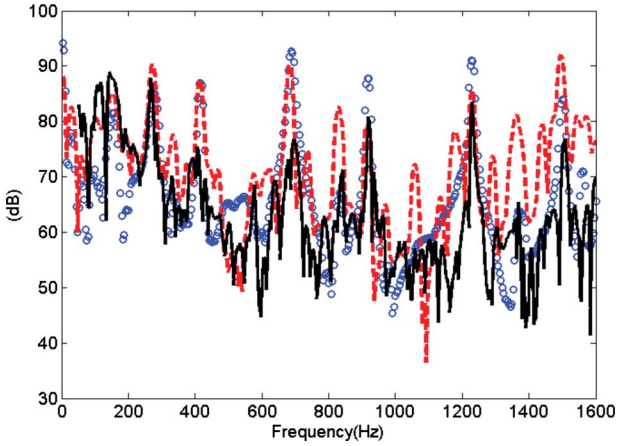

Fig. 8—Measured spatially-averaged intensity ($\bar{I}$, dB re 1.0 pW/m^2) and mean-square surface velocity ($\langle\psi_u^2\rangle_s$, dB re 5.10^{-7} m/s), on a narrow band basis. Key: Red dotted line: $\bar{I}$ by the surface intensity (I_s) method; blue circles: $\bar{I}$ by the two-microphone acoustic intensity (I_m) method; black solid line: measured mean-square velocity $\langle\psi_u^2\rangle_s$.

$$I_s(\omega) = (-1/\omega)\mathrm{Im}(G_{AP_2}(\omega)), \qquad (10)$$

where $G_{AP_2}(\omega)$ is the single-sided cross spectrum between the acceleration (A) and the pressure P_2 signals; 64 averages are taken for each spectral measurement. Here, the acoustic particle velocity at the microphone position is assumed to be the same as the surface (plate) velocity at a measurement grid point. A low mass accelerometer (2.5 grams) is used to minimize the mass loading effect. The I_s data is taken at 36 grid points of the plate like the I_m measurement. All of the surface intensity (I_s) measurements are made on a grid with 36 segments. Finally, both I_s and I_m spectra are post-processed via Matlab routines.

Concurrent with I_m and I_s measurements, the surface vibration data is recorded at 36 discrete (grid) points on the plate to determine the surface velocity amplitude U_i, averaged mean-square velocity $\langle\psi_u^2\rangle_s$, and operational deflection shapes of the plate. Figure 8 shows the measured $\bar{I}$ spectra via I_m and I_s techniques on a narrow band basis up to 1600 Hz; also, $\langle\psi_u^2\rangle_s$ spectrum is plotted. Note that a reference of 5.10^{-7} m/s is chosen for the surface velocity level so that its spectral shape (in *dB*) could be compared with the $\bar{I}$ spectra (*re* 1 pW/m^2) obtained by I_m or I_s measurements. Observe that the $\bar{I}$ based on the I_s technique closely follows the $\langle\psi_u^2\rangle_s$ spectrum. The same can only be said for $\bar{I}$ with the I_m technique for relatively narrow frequency bands spread over the measurement range.

To further examine the intensity spectra, radiation efficiency (σ_{rad}) levels (*dB re* 1) are calculated using $I(\omega) = \sigma_{rad}(\omega)\rho_o c_o\langle\psi_u^2(\omega)\rangle_s$. The radiation efficiency spectra exhibit a pattern similar to that of the intensity spectra and thus not reported here. Although discrepancies exist at some plate resonance frequencies, results are still relatively close. Yet, it is also observed that I_m based results yield a smoother spectrum with fewer sharp peaks. This might be due to a sharp gradient of the acoustic particle velocity (U_p) with distance y away from the surface where as the structural velocity (U_i) is measured by the I_s method. Other sources of error will be discussed in Sec. 6.

5 NEAR FIELD PREDICTIONS BY THE BOUNDARY ELEMENT METHOD

An indirect boundary element formulation (*Model C1*) is also employed to calculate $\bar{I}$ directly by an implicit routine[31]. In this study, results obtained via BEM are used to create a framework of predictions to compare with other results, such as from experiments or simplified models. Here, the solution to the Helmholtz equation is expressed in terms of surface potentials ($\tilde{\Phi}(x,y,z)$). A variational approach is then used to solve the integral equations that relate the unknowns, single layer (of density $\sigma_s(\tilde{p})$) monopole type sources and double layer (of density $\sigma_d(\tilde{p})$) dipole type sources $\sigma_s(\tilde{p})$ and $\sigma_d(\tilde{p})$ on S to the applicable boundaries. Gunda and Vijayakar[32,33] have discussed details of a fast multi-pole formulation and its computational efficiency. In our study, the structural dynamics of the plate is first analyzed using a finite element model with 144 elements. Then, this structural model along with the mesh is imported into the boundary element software. Surface velocity amplitudes (U_i) gathered via accelerometers are imposed (in *Model C1*) as velocity boundaries. Further, an analysis is carried out to ensure whether the number of elements used in the structural finite element model is sufficient for predicting the near-field pressures. To accomplish this, the intensity radiated by the plate is directly found by a built-in intensity routine within the boundary element software[31–33].

Next, the same boundary element method is then utilized to simulate two pressures at y_1 and y_2 (as shown in Fig. 3), and estimate the $\bar{I}$ spectrum like the two-microphone acoustic intensity (I_m) experiment (as described in Sec. 4). This particular model is designated as *Model C2*. The aim is to see if any near field measurement errors could be identified. In our work, pressures P_1 and P_2 are estimated at y_1 and y_2 (like the

Table 2—Comparison of $\bar{I}$ values obtained via experimental and analytical methods at the resonance frequencies of the plate.

Spatially-Averaged Intensity (dB re 1 pW/m^2) at Dominant Resonances						
	Plate Resonance Frequency (Hz)					
Method (Measured or Predicted)	276	420	688	920	1232	1504
Measured by I_m	82.1	75.1	76.9	83.7	86.9	80.8
Measured by I_s	75.4	87.7	89.5	78.9	85.6	88.6
Predicted by *Model A1* (Piston Radiator without mutual interaction)	88.7	87.8	88.8	97.1	96.3	90.3
Predicted by *Model A2* (Piston radiator with mutual interaction)	79.0	74.4	75.7	81.9	84.4	79.6
Predicted by *Model B* (Pulsating sphere)	97.5	86.6	96.8	105.4	103.5	97.6
Predicted by *Model C1* (Indirect BEM)	84.4	81.5	86.5	94.6	101.2	94.7
Predicted by *Model C2* (I_m simulated using BEM)	85.2	82.0	86.4	94.4	101.4	94.4

I_m measurements), with $\Delta y = 18$ mm, and $y = 17$ mm (distance from plate to the acoustic center of microphones as shown in Fig. 3). The particle velocity (U_p) is estimated by calculating the single-sided cross power spectrum as $G_{P_2P_1}(\omega) = P_2^*(\omega)P_1(\omega)$, instead of using the finite difference formula. Acoustic intensity (I_m) spectrum is then calculated by using Eqn. (9).

6 COMPARATIVE RESULTS AND SOURCES OF ERROR

Results from 5 models and 2 experiments are compared in Table 2 and Fig. 8. First, we examine the spatially-averaged intensity levels (in Table 2) at resonance frequencies of the plate since they dominate the spectra as seen in Fig. 8. Further, natural frequencies of this plate are calculated by using the finite element method, and the dominant resonance frequencies are found to be close (say within 5%) to the measured ones. They are compared with measured resonance frequencies in Table 3.

Many more natural modes (including repeated roots given the symmetric nature of the plate) are of course obtained in the finite element analysis but only certain modes (as mentioned above) are excited in the experiment. As shown in Fig. 8, the narrow band intensity spectra are dictated by the plate resonances and anti-resonances. In order to have a greater clarity in the comparisons and to emphasize the role played by resonances (dominant sources), sound intensities are next converted to 1/3 octave band basis in the post-processing mode. All models and both measurements are compared in Fig. 9 from 50 to 1600 Hz bands. Predictions of *Model A2* are relatively closer to the measurement (both I_m and I_s) results when compared with other models. The reason is that *Model A2* carries the same phase information as the I_s measurements, via the mutual impedance terms. Thus, *Model A2* incorporates the "acoustic short cuts" between neighboring anti-phase radiators. It is also observed that the mutual resistance is as important as the self-resistance (in our analysis when $\Gamma/2 < 0.4$). Further, the mutual reactance in the near field ($0 \leqslant \Gamma/2 \leqslant 1$) is found to be less important than the mutual resistance.

The boundary element methods (*Models C1 and C2*)

Table 3—Comparison of resonance frequencies of the square plate obtained via finite element method (FEM) and measurements.

Resonance frequencies of the plate (Hz)						
Finite Element Method	247	411	676	919	1218	1486
Measurement	276	420	688	920	1232	1504

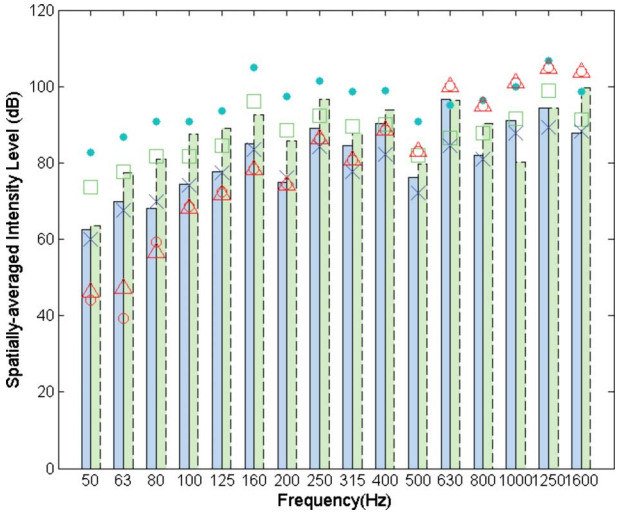

Fig. 9—Comparison of measured (given by bars) and predicted (given by discrete symbols) spatially-averaged intensity levels $\bar{I}$, dB re 1.0 pW/m^2 on 1/3 octave band basis. Key: Green bars: measured by the surface intensity (I_s) method; blue bars: measured by the two-microphone acoustic intensity (I_m) method; green open squares: predicted by Model A1; blue crosses: predicted by Model A2; blue solid circles: predicted by Model B; red open circles: predicted by Model C1; red open triangles: predicted by Model C2.

yield almost the same $\bar{I}$ spectrum. Overall, the boundary element methods suggest possible errors committed by the two-microphone method when carried out in a non-ideal acoustic environment, while also confirming that sufficient number of segments (meshes) is used in discrete analytical models. Note that the predictions of *Model C1* are closer to the spectrum obtained via the I_m measurement below 350 Hz than to the spectrum obtained via the I_s method. In the higher frequency range, measurements are closer to *Model A1* results or even to the pulsating sphere formulation (*Model B*). This suggests that boundary element formulation uses single-layered monopole type sources in the higher frequency range.

Next, we discuss the reasons for discrepancies between measurements themselves and between experimental and predicted spatially-averaged intensities. First, both surface and two-microphone intensity measurements are carried out in the near field where the acoustic field is mostly reactive. Consequently, resistive intensities are very low at or near the anti-resonance frequencies even though the sound pressures remain high. Thus, the acoustic intensity spectrum exhibits sharper minimums at the anti-resonance frequencies of the plate. Pressure-intensity index ($\delta_{PI}=L_p-L_I$) spectrum for each measurement reveals that up to 20 dB values are seen at the lower frequencies (below 350 Hz) where some rigid body motions are observed. This might be the reason for relatively large differences between models and experiments in the lower frequency region. Second, recall that the structural frequency response functions (and thus velocities and intensities) from $N=36$ different regions are spatially averaged to give the total intensity spectra ($\bar{I}$). The frequency response functions contribute more to surface vibration measurements than the sound field related measurements. Thus, in some regions, measured spectra have serious discrepancies. These errors might be less to some extent when more discrete segments (discrete sources) on the plate are employed.

In the two-microphone (acoustic) intensity method (I_m), finite difference errors could be significant when the microphone separation distance is approximately equal to the distance of the measurement location (y) from the source[34]. Here, in our study, they are almost equal ($\Delta y=18$ mm and $y=17$ mm); this would pose the finite difference approximation error as a dominant source of discrepancy. Experimentally, the plate is attached to a stinger via a bolted connection where the nut and a small portion of the stinger extend above the top surface of the plate. Thus, near field conditions corresponding to the segment in the middle of the plate are not exactly achieved at the mid-point of this segment. Moreover, the bolted connection itself would disturb the near field radiation field. As this particular segment is expected to be one of the most efficient radiation regions of the plate, measurements might have been underestimated because of aforementioned reasons. For the surface intensity measurements (I_s), a miniature accelerometer is attached on the discrete partitions in the middle of each partition and a microphone is placed in its close proximity. Besides, accelerometer might have disturbed the sound field contaminating the information captured by the microphone, while causing some mass loading at higher frequencies. Further, there is a phasing problem in this measurement technique as one sensor gathers data from a dispersive wave medium where the other one from a non-dispersive wave medium.

Finally, the near field two-microphone acoustic intensity (I_m) measurements are carried out only on the top of the unbaffled plate. However, our computational study (based on the BEM, *Model C1*) indicates that edges and back side might be important as well. Results are reported in Fig. 10. For instance, the edges contribute to the overall radiation more than we had presumed in the lower frequency range. Also, some cancellations are seen at low frequencies when the

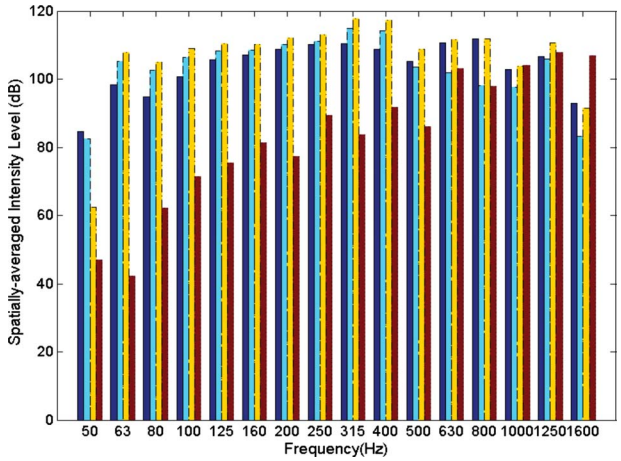

Fig. 10—Contribution of spatially-averaged intensity level $\bar{I}$, dB re 1.0 pW/m^2, from different regions of the plate on 1/3 octave band basis. Key: Dark blue bars: from the plate center; light blue bars: from the plate corners; yellow bars: from the plate edges (including the corners), red bars: from the top surface of the plate.

radiation from the top plate is examined. That suggests the importance of measurements from sides as well as from the bottom of the plate which were obviously not made in the original experimental study.

7 CONCLUSION

Three analytical formulations (*A1, A2 and B*) used in our study are assumed to be discretized radiation sources (each radiating in an infinite baffle). Note that the discrete models carry the phase information obtained via surface vibration measurements. However, the baffled conditions are not achieved especially for source segments at or near the edges and corners. Further, *Models A1 and B* assume that the sources radiate into a half-sphere independent from each other, e.g. without any acoustic interaction. Such discrete radiators are based on the premise that they convert all vibratory energy in to the sound mode. Moreover, these discrete sources do not carry any directivity information as they radiate equally in the radial direction within a hemi-spherical radiation surface. Nonetheless, results of the piston radiator formulation with mutual impedances (*Model A2*) are relatively closer to the acoustic intensity measurements. The boundary element method (*C1 and C2*) predicts only the acoustic field and thus its predictions are similar to the acoustic intensity measurements at least over the lower frequency range. Even though predictions and measurements do not perfectly match, this paper clearly demonstrates that the mutual radiation resistance terms (in the near field of a vibrating free-free plate) are as important as the self radiation resistance terms. For instance, *Model A1 and Model B* overestimate the spatially-averaged intensity spectra. Besides, results obtained via *Model A2* are much closer to the acoustic intensity results. This suggests the importance of incorporating mutual impedance terms when predicting the near fields of such acoustic sources. However, even the results from Model A2 are not very close to the experimental results at some frequency ranges. Consequently, one should utilize both analytical and computational (such as boundary element) models to investigate the near field acoustics. A higher dimensional analytical or hybrid model might be efficient though more vibration measurements (including phases) would be needed. Finally, we encourage researchers to examine the near fields of typical plate radiators with emphasis on resonant vibrations and share their analytical and experimental results. Collective efforts would lead to some benchmark solutions that are needed by the practitioners.

8 ACKNOWLEDGMENTS

The authors wish to thank Rajendra Gunda of the Ansol Inc., Hilliard Ohio for providing access to the BEM software *Coustyx*[31] and for technical discussions.

9 REFERENCES

1. F. J. Fahy and P. Gardonio, *Sound and Structural Vibration: Radiation, Transmission and Response*, Academic Press, London, (2007).
2. N. Atalla and J. Nicolas, "A new tool for predicting rapidly and rigorously the radiation efficiency of plate-like structures", *J. Acoust. Soc. Am.*, **95**(6), 3369–3378, (1994).
3. M. F. Jacobsen, R. Singh and F. B. Oswald, "Acoustic Efficiency Models of a Simple Gearbox", Army Research Laboratory Technical Report, ARL-TR-1111, (1996).
4. W. L. Lee and H. J. Gibeling, "Determination of the mutual radiation resistances of a rectangular plate and their impact on the radiated sound power", *J. Sound Vib.*, **229**(5), 1213–1233, (2000).
5. T. Takahagi, M. Nakai and Y. Tamai, "Near field sound radiation from simply supported rectangular plates", *J. Sound Vib.*, **185**(3), 455–4713, (1995).
6. F. Cervera, H. Estelles, F. Galvez and F. Belmar, "Sound intensity in the near field above a vibrating flat plate", *Noise Control Eng. J.*, **45**(5), 193–199, (1997).
7. L. Shuyu, "Study on the radiation acoustic field of rectangular radiators in flexural vibration", *J. Sound Vib.*, **254**(3), 469–479, (2002).
8. D. J. Gorman, "Free Vibration Analysis of Completely Free Rectangular Plates by the Superposition-Galerkin Method", *J. Sound Vib.*, **237**(5), 901–914, (2000).
9. D. J. Gorman, "Free In-plane Vibration Analysis of Rectangular Plates by the Method of Superposition", *J. Sound Vib.*, **272**, 831–851, (2004).
10. L. Shuyu, "Study on the Flexural Vibration of Rectangular Thin Plates with Free Boundary Conditions", *J. Sound Vib.*, **239**(5), 1063–1071, (2001).
11. H. L. Kuntz, "Radiated sound and the geometric nearfield size",

Noise Control Eng. J., **56**(4), 269–281, (2008).
12. J. B. Fahnline and G. H. Koopmann, "A lumped parameter model for the acoustic power output from a vibrating structure", *J. Acoust. Soc. Am.*, **100**(6), 3539–3547, (1996).
13. J. B. Fahnline and G. H. Koopmann, "Numerical implementation of the lumped parameter model for the acoustic power output of a vibrating structure", *J. Acoust. Soc. Am.*, **102**(1), 179–192, (1997).
14. N. Hashimoto, "Measurement of sound radiation efficiency by the discrete calculation method", *Appl. Acoust.*, **62**, 429–446, (2001).
15. G. Zhen, W. Zhongzhang and G. Tun, "Relation between plate vibration and its sound field", *Noise Control Eng. J.*, **32**(1), 35–41, (1989).
16. G. H. Koopmann and J. B. Fahnline, *Designing Quiet Structures*, Academic Press, California, (1997).
17. S. G. Hill, S. D. Snyder and N. Tanaka, "Acoustic based sensing of orthogonal radiating functions for three-dimensional noise sources: Background and experiments", *J. Sound Vib.*, **318**, 1050–1076, (2008).
18. E. Skudrzyk, *The Foundations of Acoustics*, Springer-Verlag, New York, (1971).
19. P. M. Morse and K. U. Ingard, *Theoretical Acoustics*, Princeton University Press, Princeton, New Jersey, (1987).
20. J. W. S. Rayleigh, *The Theory of Sound: Volume 2*, Dover Publishers Inc., New York, (1945).
21. D. T. Blackstock, *Fundamentals of Physical Acoustics*, John Wiley & Sons, Inc., New York, (2000).
22. R. L. Pritchard, "Mutual acoustic impedance between radiators in an infinite rigid baffle", *J. Acoust. Soc. Am.*, **32**(6), 730–737, (1960).
23. H. Lee, J. Tak, W. Moon and G. Lim, "Effects of mutual impedance on the radiation characteristics of transducer arrays", *J. Acoust. Soc. Am.*, **115**(2), 666–679, (2004).
24. R. M. Aarts and A. J. E. M. Janssen, "Approximation of the Struve function H1 occurring in impedance calculations", *J. Acoust. Soc. Am.*, **113**(5), 2635–2637, (2003).
25. P. R. Stepanishen, "An approach to computing time-dependent interaction forces and mutual radiation impedances between pistons in a rigid planar baffle", *J. Acoust. Soc. Am.*, **49**(1), 283–292, (1971).
26. L. E. Kinsler, A. R. Frey, A. B. Coppens and J. V. Sanders, *Fundamentals of Acoustics*, John Wiley & Sons, New York, (2000).
27. P. R. Stepanishen, "Evaluation of mutual radiation impedances between circular pistons by impulse response and asymptotic methods", *J. Sound Vib.*, **59**, 221–235, (1978).
28. F. J. Fahy, "Measurement of acoustic intensity using the cross-spectral density of two microphone signals", *J. Acoust. Soc. Am.*, **62**(4), 1057–1059, (1977).
29. T. H. Hodgson, "Investigation of the surface acoustical intensity method for determining the noise sound power of a large machine in situ", *J. Acoust. Soc. Am.*, **61**(2), 487–493, (1977).
30. P. L. Driesch, H. Iwata, G. H. Koopmann and J. Dosch, "Development and evaluation of a surface acoustic intensity probe", *Rev. Sci. Instrum.*, **71**(10), 3947–3952, (2000).
31. R. Gunda, *Coustyx Analytical Manual*, Ansol Inc., Hilliard, Ohio, USA, (2007).
32. R. Gunda and S. Vijayakar, "Acoustic radiation from an automotive gearbox", *SAE Noise and Vibration Conference*, Paper No: 2007-01-2170, (2007).
33. R. Gunda, "Boundary element acoustics and the fast multipole method (FMM)", Sound and Vibration, 12–16, (March 2008).
34. G. Steyer, "Spectral Methods for the Estimation of Acoustic Intensity, Energy Density, and Surface Velocity using a Multimicrophone Probe", Ph.D. Thesis, The Ohio State University, (1984).